Proceedings of the Tenth Pacific Conference on Earthquake Engineering
Building an Earthquake-Resilient Pacific
6-8 November 2015, Sydney, Australia

Damage detection in the 2015 Nepal earthquake using ALOS-2 satellite SAR imagery

W. Liu & F. Yamazaki

Chiba University, Chiba, Japan.

ABSTRACT: The Mw 7.8 earthquake jolted the central region of Nepal on April 25, 2015, and caused gigantic destruction. Satellite remote sensing is an effective tool to grasp damages in a wide area. In this study, pre- and post-event ALOS-2 satellite SAR data were used to detect affected areas in Kathmandu, the capital city of Nepal. Firstly, the crustal movements around the Kathmandu Valley were estimated by the interferometric SAR (InSAR) analysis using a pre- and post-event pair data. Due to the large fault plane of the earthquake, significant displacements occurred in the whole valley. More than 1 m movements to the line-of-sight direction were obtained in the target area. Then the damaged areas in the centre of Kathmandu were detected by three different indices. First one is the normalized difference coherence index, calculated from both the amplitude and phase information of SAR echo. Second and third indices were calculated from only the amplitude information based on differences and correlation coefficients. Comparing with optical satellite images, all the indices showed good capability in damage extraction at an emergency response phase.

1 INTRODUCTION

An Mw 7.8 earthquake hit Nepal at 11: 56 am on April 25, 2013. The epicentre was located at 28. 23° N, 84.73° E, with a shallow focal depth of 8 km. This earthquake was caused by thrust faulting between the subducting India Plate and the overriding Eurasia Plate. According to the fault model calculated from seismic waveforms by USGS, the causative fault plane is 20 km in length and 15 km in width with 295-degrees strike angle and 10-degrees dip angle. Due to the strong motion in a wide area, it became the worst natural disaster in Nepal since the 1934 Bihar, Nepal earthquake. More than 8,600 people were killed in Nepal and 161 people in the surrounding countries due to building collapses, landslides and avalanches triggered by the strong shaking. Thousands of houses were destroyed and more than 450,000 people were displaced. Several famous monuments, such as pagodas in Kathmandu Durbar Square and Dharahara tower, were collapsed and killed many tourists. Since the Tribhuvan International Airport was closed immediately after the earthquake and a number of roads were suffered from landslides, international aid activities and field reconnaissance surveys were difficult to carry out.

Remote sensing is recognized as an efficient tool to monitor a wide range of natural disasters by optical and radar sensors. Optical images can easily capture detailed ground surface information, but the approach is limited by weather conditions. In contrast, synthetic aperture radar (SAR) sensing is independent of weather and daylight conditions, and thus more suitable for damage mapping reliably and promptly. Due to remarkable improvements in radar sensors, high-resolution COSMO-SkyMed, TerraSAR-X and ALOS-2 (PALSAR-2) images are available with ground resolution of 1 to 5 m, providing detailed surface information.

There has been many researches working on rapid damage assessment after natural disasters using SAR data. Interferometric analysis is one of the most powerful methods to detect crustal movements and also to investigate building damages (Stramondo et al., 2002; Michele et al., 2010; Ito et al., 2000; Yonezawa and Takeuchi, 2001). Matsuoka and Yamazaki (2004) performed a feasibility study on the backscattering characteristics of damaged areas in the 1995 Kobe, Japan earthquake, and developed an automated method to detect hard-hit areas using ERS SAR intensity images. The proposed method was also applied to Envisat ASAR images in the 2003 Bam, Iran earthquake (Matsuoka and Yamazaki, 2005). Recently, several studies attempted to detect damage at the scale of a single building unit, using both high-resolution optical and SAR images (Brunner et al., 2010; Wang and Jin, 2012).

ALOS-2 (also called “Daichi-2” in Japanese) with an enhanced synthetic aperture radar (SAR) PALSAR-2 sensor is the only one L-band SAR satellite in the world, succeeding ALOS PALSAR. It contributes to cartography, regional observation, disaster monitoring and resource surveys. The satellite was launched on May 24, 2014, with the 4 days repeat period. There are three modes for the acquisition, the Spotlight mode with 1 to 3 m resolution, the Strip Map mode with 3 to 10 m resolution and the Scan SAR mode with 350 km or 490 km swath width. Both the single polarization and the combination of co- and cross-polarizations are available by the PALSAR-2 sensor. The improvement of the observation frequency and the spatial resolution allows more comprehensive monitoring of disasters.

In this study, two pre- and one post-event pairs of ALOS-2 PALSAR-2 are used to estimate crustal movements and building damages caused by the Nepal earthquake. The crustal movements in a wide-range are estimated by the InSAR analysis first. Then the damaged areas in the centre of Kathmandu are detected by three different indices. The normalized difference index for the coherence (NDCI) and that for the correlation coefficient (NDCOI) are calculated by the combination of the pre-event pair and the pre-, post-event pair. The Z factor, which includes both the difference and correlation coefficient between the pre- and post-event intensity data, is also introduced for damage detection. Finally, the accuracy of our results is verified by comparing with optical satellite images.

2 STUDY AREA AND IMAGE DATA

The study area focuses on the capital city, Kathmandu, as the red frame shown in Fig. 1(a). The location of the fault plane and the epicentre determined by USGS is also shown in Fig. 1(a) by the blue frame and the star mark (USGS, 2015). The background colours represent ShakeMap in terms of the Modified Mercalli intensity (MMI). Most of the target area is located in the strong seismic intensity more than VI. Two pre-event and one post-event PALSAR-2 data were used in study. The pre-event images were taken on October 4, 2014 and February 21, 2015 whereas the post-event image was taken on May 2, 2015, one week after the mainshock. The observation conditions of the three data were almost the same, the incident angle 35.3° at the centre of the images, with a heading of 344° clockwise from the north. All the data were captured with horizontal/horizontal (HH) and horizontal/vertical (HV) polarizations in the Fine Beam Dual (FBD) mode. The resolution was 7.2 m in the azimuth direction and 4.3 m in the slant range direction.

The three imagery data were provided as the range and single-look azimuth compressed data with the processing level 1.1, which were represented by the complex I and Q channels to preserve the amplitude and phase information. Several pre-processing steps were carried out using *ENVI/SARscape* software.

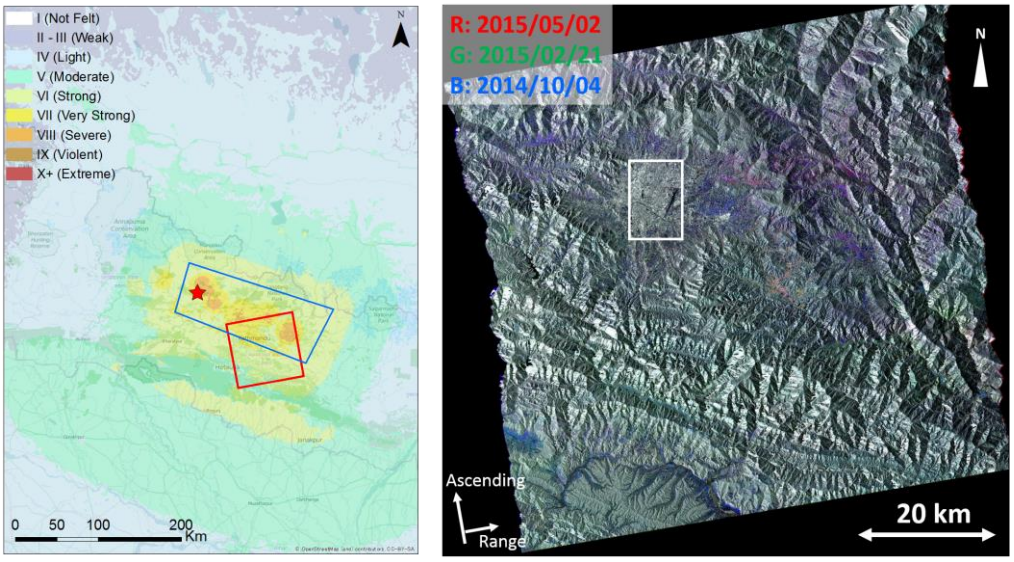

(a) (b)

Fig. 1 Location of the study area around Kathmandu and the fault plane by USGS, overlapping on the MM intensity contour map (a); a colour composite of two pre-event and one post-event PALSAR-2 intensity images in the HH polarization, geocoded into UTM projection (b).

A multi-looking process was applied to the range direction, and then the resolution in the slant-range direction was changed to 8.6 m. A 90 m Shuttle Radar Topography Mission (SRTM) digital elevation model (DEM), was introduced to project the data to a WGS84 reference ellipsoid with a resampled square pixel size of 10 m. Radiometric calibration was also carried out to transform the amplitude data into the backscattering coefficient (sigma naught) values. After applying a speckle-noise reduction filter, a colour composite image of the two pre-event and one post-event intensity images in the HH polarization was generated and shown in Fig. 1(b). Significant changes in the backscattering intensity could be confirmed in the mountain area due to seasonal changes (vegetation and snow).

The close-up of Kathmandu (the white square in Fig. 1(b)) is shown in Fig. 2 by the colour composites of the HH and HV polarizations. According to the different backscattering characteristics, vegetation areas could be identified by green colour whereas built-up areas show magenta colour. The Bagmati River, the runway of the Tribhuvan International Airport and the ground of Tundikhel show the lowest backscatter due to their smooth surfaces. Although several severe damages were reported in the city, it is difficult to identify them by visual inspection of these intensity images.

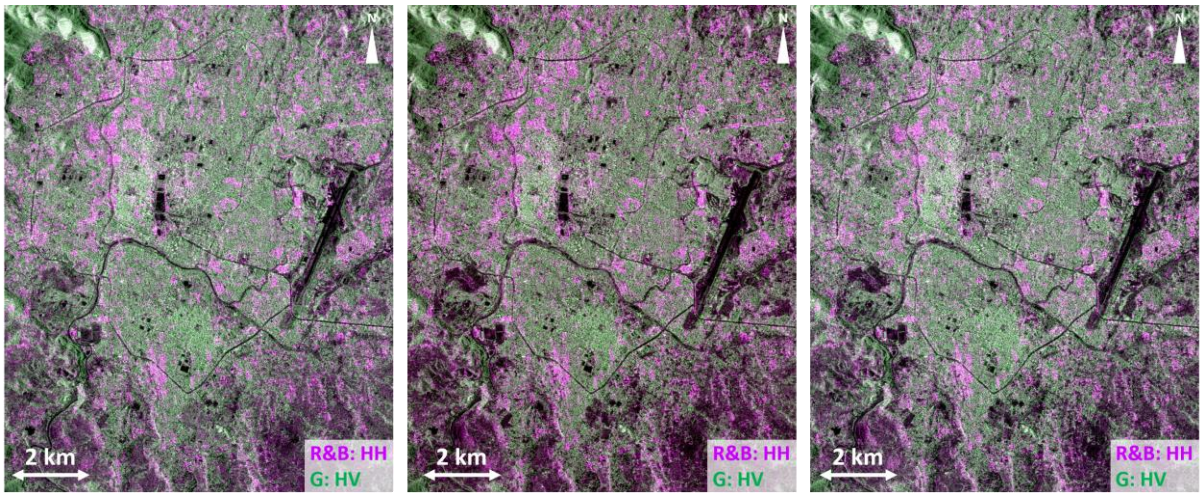

(a) Oct. 4, 2014 (b) Feb. 21, 2015 (c) May 2, 2015

Fig. 2 Colour composites of the HH and HV polarizations for three different periods respectively.

3 ESTIMATION OF CRUSTAL MOVEMENTS

InSAR analysis is a radar technique, which is used to generate maps of surface deformation or digital elevation, using the phase differences of the radar waves between two- or multi-temporal SAR data. An InSAR analysis was applied to the three complex-data products of PALSAR-2 using *ENVI/SARscape* software. First, an initial InSAR result was obtained using the two complex imagery data. The SRTM DEM was introduced to remove elevation and orbital effects from the initial result. In this stage, noises were removed by the Goldstein filter (Goldstein and Werner, 1998). Then the final interferogram including only the fringe caused by coseismic deformation was obtained. In addition, the coherence, which represents the quality of interferogram, was calculated with the value between 0 and 1. Finally, the final interferogram and coherence values were projected on a geo-referenced map.

The temporal difference between the two pre-event data was 140 days whereas that of the second pre-event and post-event data was 70 days. The spatial baseline distances of the two pairs were 178 m and 119 m, respectively. The both pairs show high coherence. Excepting a subsidence area observed in the northwest part of Kathmandu, no other significant movement was seen in the pre-event interferogram. The subsidence was also observed from the co-event pair, which might be caused by the underground water-table change. The final interferogram for the co-event pair is shown in Fig. 3(a). The fringe caused by the coseismic deformation between $-\pi$ and π was obtained from the areas with higher coherence than 0.2. One cycle represents 11.8 cm displacement, which is a half of the wavelength of the L-band radar. Counting from the southwest, 12 cycles of fringes could be identified in the target areas, which represents the displacement of 1.4 m to the range direction.

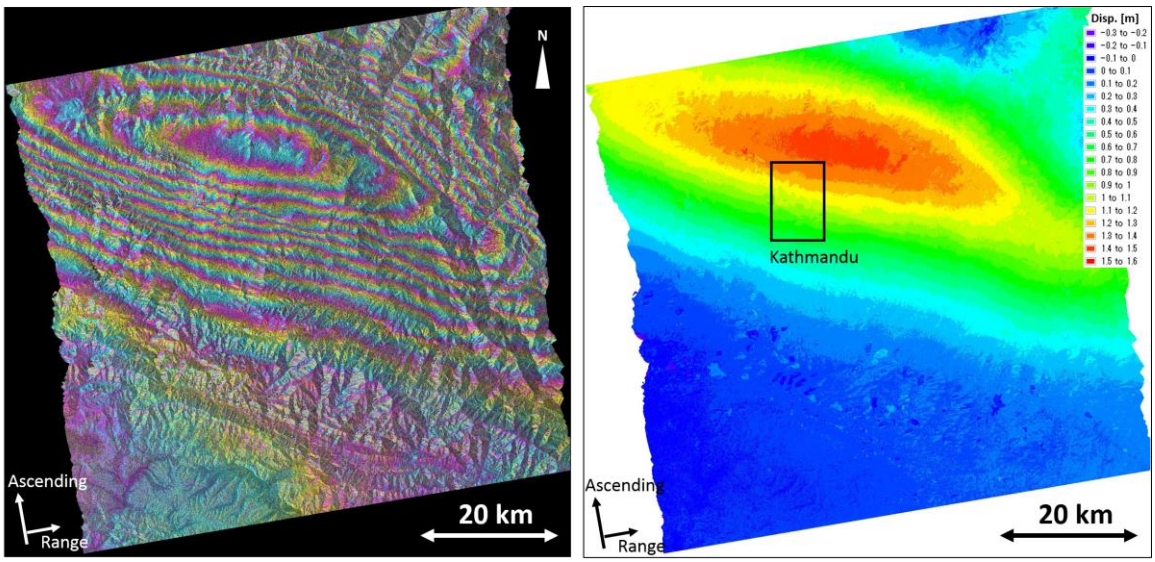

(a) (b)

Fig. 3 Fringe caused due to coseismic deformation obtained by removing orbit fringe, topographic fringe and noises from the initial interferogram (a); the displacements in the line-of-sight direction, detected by unwrapping the fringes obtained from the InSAR analysis (b).

An unwrapping step was carried out to connect discontinuous fringes into a continuous displacement. The fringes in the whole target area with higher coherence values than 0.25 were unwrapped by the Minimum Cost Flow method (Costantini, 1998). To remove the phase offset, ground control points (GCPs) were required after unwrapping. Normally, the locations and observed records of GPS stations are used as GCPs. However, there is no available GPS data in this area. Moreover the deformation occurred in the entire imaging area. Thus, only one point was assigned as the stable (fixed) reference point at the southwest corner of the SAR image. The displacements in the line-of-sight direction were obtained and shown in Fig. 3(b). Since the target area covers a half of the fault plane, the most parts showed the movements to the same direction, as forward to the sensor direction. The maximum value of the obtained displacements was 1.56 m, matching with the visual counting. The city area of Kathmandu is shown in the black frame, where the deformations were in the range from 0.5 m to 1.3 m. Since the displacements in Kathmandu are in the same direction, no significant surface rupture was expected in the area.

4 DAMAGE DETECTION IN KATHMANDU CITY

4.1 Normalized difference coherence index (NDCI)

The pre- and the co-event coherence values were calculated in the slant range images from the complex data in the InSAR analysis. The pre-event coherence (γ_a) was obtained from the images taken on Oct. 4, 2014 and Feb. 21, 2015, whereas the co-event coherence (γ_b) was obtained from the images taken on Feb. 21 and May 2, 2015. The pre- and co-event coherence values in Kathmandu City are shown in Fig. 4(a-b). The coherence is influenced by the temporal distance, the baseline distance, the surface changes and noises. Although the baseline decorrelation can be calculated easily, the temporal decorrelation is difficult to calibrate. Since the both baseline distances were less than 200 m, the baseline decorrelation could be ignored in this study. However, the temporal distance of the pre-event pair was twice of that of the co-event pair. Thus, the pre-event coherence showed lower values in most parts of the built-up area.

To estimate an accurate decrease in coherence caused by the earthquake, a normalized difference coherence index (*NDCI*) was calculated by Eq. (1) and shown in Fig. 5(a).

$$NDCI = \frac{\langle \gamma_a - \gamma_b \rangle}{\langle \gamma_a + \gamma_b \rangle} \tag{1}$$

where, < > represents a smoothing window with 7×7 pixels.

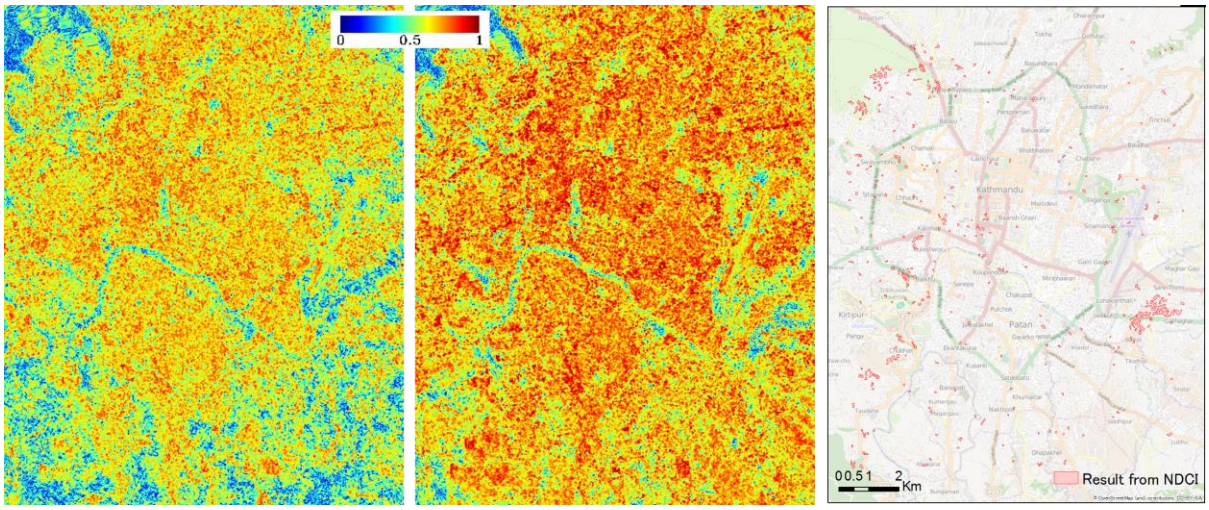

(a) pre-event coherence (b) co-event coherence (c) suspicious damaged areas

Fig. 4 Pre- (a) and co-event (b) coherence obtained by InSAR analysis; the detected suspicious damaged areas using the positive *NDCI* values (c).

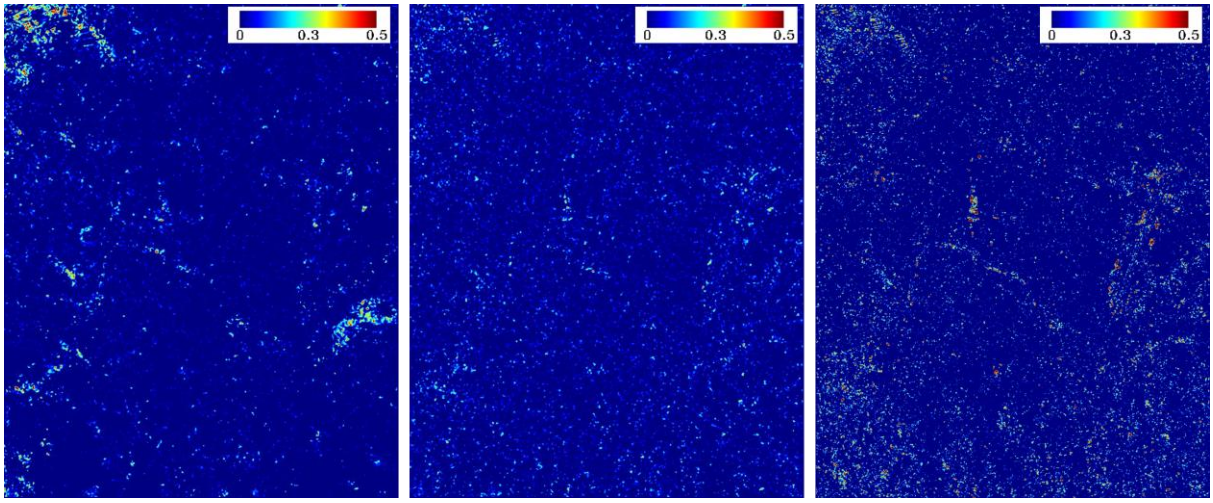

(a) *NDCI* (b) *NDCOI* (c) *Z* factor

Fig. 5 Three indices used for damage detection: *NDCI* (a), *NDCOI* (b) and *Z* factor (c), respectively.

Since the pre-event coherence is lower than the co-event one, the most of the area show negative values. Only several damaged areas show positive values due significant changes caused by the earthquake. However, two largest changed areas in the southeast and the northwest are due to the change of vegetation. To remove these errors in damage detection, a mask was applied based on the pre-event coherence. The areas with higher coherence than 0.5 were extracted as built-up ones whereas the others were considered as vegetation and masked from the *NDCI* values. Then the positive *NDCI* pixels were extracted as building damages. The pixels with higher value than 0.1 were extracted and grouped into objects. Considering the smoothing window size of 7×7 pixels, the objects smaller than 64 pixels were removed as noises. The finally obtained damage map is shown in Fig. 4(c). An area of about 1.4 km^2 was extracted. Although the low pre-event coherence pixels have been masked, vegetation with high coherence before the earthquake still existed in the result.

4.2 **Normalized difference correlation index (NDCOI) and *Z* factor**

The changes of the correlation coefficient were also calculated to detect affected areas. Different from the coherence, the correlation coefficient was obtained from the ground range intensity images. The pre-event correlation coefficient (C_a) was calculated from the sigma naught backscattering images on Oct. 4, 2014 and Feb. 21, 2015, whereas the co-event coefficient (C_b) was calculated from the images on Feb.

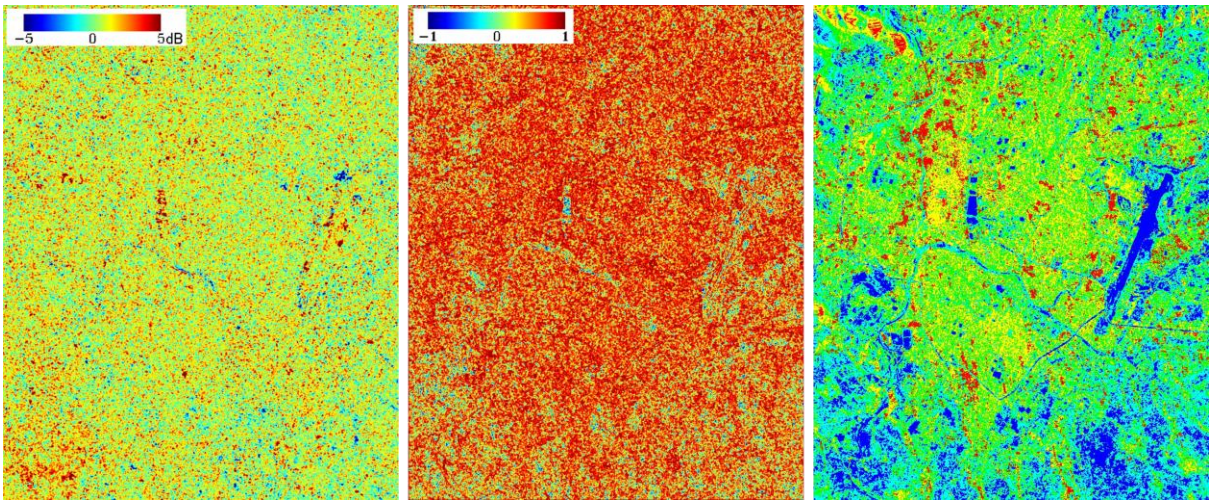

(a) co-event difference (b) co-event correlation coefficient (c) unsupervised classification

Fig. 6 Co-event difference (a) and co-event correlation (b) of backscattering coefficient (sigma naught) values and the result of unsupervised classification with five classes (c).

21 and May 2, 2015. The co-event correlation is shown in Fig. 6(b) with high correlation. Due to the seasonal difference, the pre-event correlation also show lower values than the co-event one. The normalized difference correlation index (NDCOI) was obtained by Eq. (2) and shown in Fig. 5(b). Since the C_a and C_b were between -1.0 and 1.0, they were added 1 to move into the positive-value range, between 0 and 2.

$$NDCOI = \frac{\langle C_a - C_b \rangle}{\langle C_a + C_b + 2 \rangle} \tag{2}$$

Because the pre- and post-event correlation coefficients were similar, no significant changes was observed in the *NDCOI* map. However, the areas with positive values higher than 0.1 were extracted and grouped into objects.

Since the PALSAR-2 data used in this study have two polarizations, an unsupervised classification was applied on the image taken on Feb. 2, 2015 to extract pre-event built-up areas. The image shown in Fig. 3(b) was classified into 5 classes as shown Fig. 6(c). From the lowest to the highest backscatter, the classes are assigned as blue, cyan, green, yellow and red. The blue class represents the smooth surfaces such as airport runways or paddy fields. The cyan class represents vegetated areas with low grasses. Thus, only possible built-up areas were extracted using the three brightest classes. After applying this non-urban mask, the detected damaged areas are shown in Fig. 7(a) by blue polygons. 0.89 km^2 areas were extracted, smaller than the result from the *NDCI* values.

The present authors proposed a new index, the *Z* factor, for monitoring urban changes, using the difference and correlation coefficient (Liu and Yamazaki, 2015). This factor was also introduced in this study for damage detection. The *Z* factor for the image on Feb. 21 and May 2, 2015 was calculated by Eq. (3), using the difference and correlation coefficient shown in Fig. 6(a-b). When the weight of the correlation coefficient is assigned as 0.5, the *Z* factor is in the range between -0.5 and 1.5. A high value represents a high possibility of change. The obtained *Z* factor is shown in Fig. 5(c).

$$Z = \frac{|D|}{\max|D|} - w \times C \tag{3}$$

where *D* is the difference and *C* is the correlation coefficient, | | represents the absolute value, and *w* is the weight factor, which is 0.5 in this study.

Comparing with the *NDCI* and *NDCOI* values, Z factor show higher value in the Tribhuvan International Airport and Tundikhel district. The same approach was carried out to detect the damaged areas using the *Z* factor. After applying the urban mask obtained by the classification, the areas with higher value than 0 were extracted and show in Fig. 7(a) by magenta polygons. A total of 2.60 km^2 areas were

identified as suspicious damaged areas.

To verify our results obtained from the three different indices, comparison of our results with optical satellite images was carried out. The pre- and post-event Pleiades satellite images were employed for this purpose. Airbus Defence and Space provided these data to support the International Charter and Copernicus Emergency Management Service. The pre-event image was acquired on November 29, 2014 whereas the post-event one on April 27, 2015, two days after the mainshock. Fig. 7(b) show our results overlapping on the post-event Pleiades image around Tundikhel district, including famous Kathmandu Durbar Square and Dharahara tower. The result from the *NDCOI* value is smallest and covered with the result from the *Z* factor.

A more detailed comparison was made for four selected areas shown in Fig. 8 using the pre- and post-event Pleiades satellites and our extracted results. Location *a* is the Kathmandu Durbar Square. Four

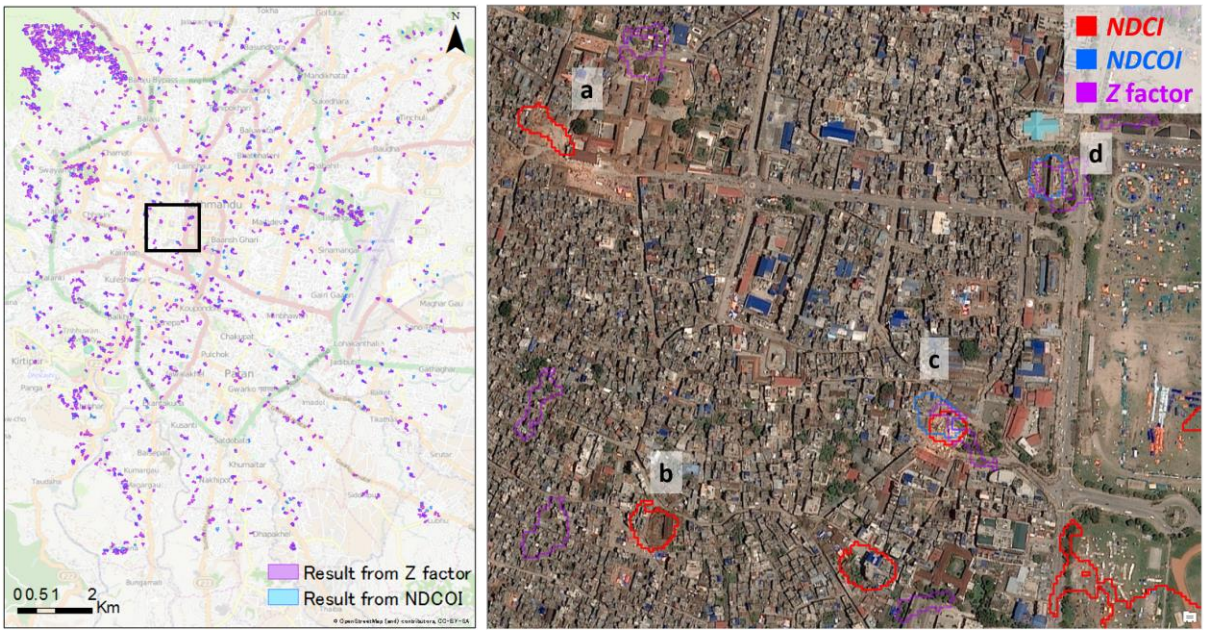

(a) (b)

Fig. 7 Detected suspicious damaged areas using the positive *NDCOI* and *Z*-factor values (a); the extracted areas from three indices overlapping on the post-event Pleiades taken on April 27 ,2015 (b).

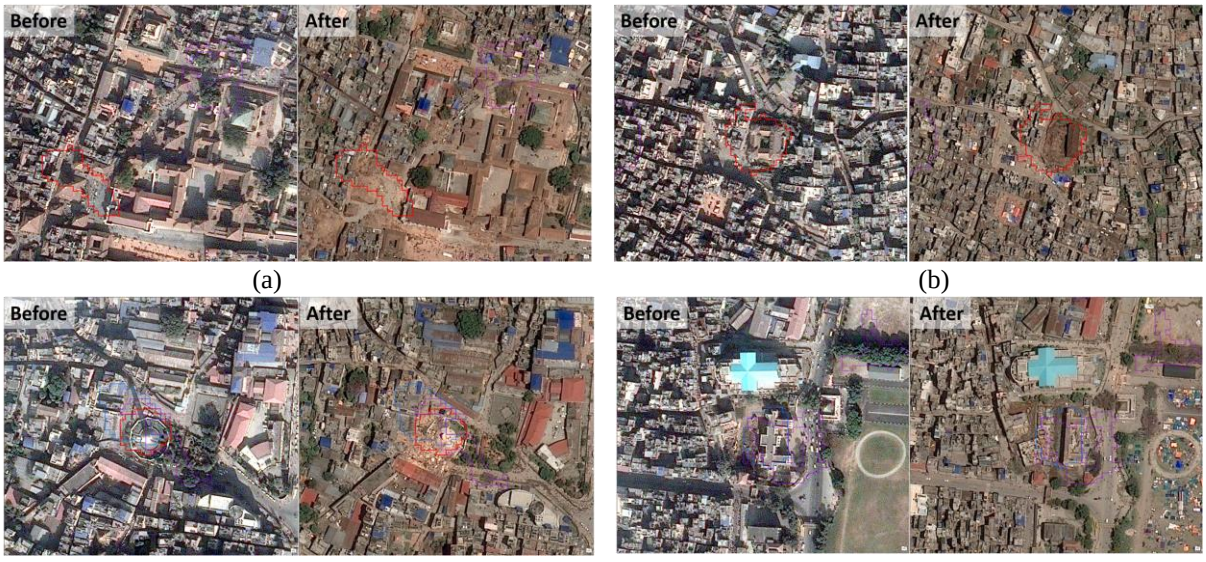

(a) (b)

(c) (d)

Fig. 8 Comparisons of the obtained results by three indices and the pre- and post-event Pleiades optical images at four locations. (a-d) corresponds to the location a-d shown in Fig. 7 (b).

pagodas were completely collapsed in the southwest part of the square. Comparing with our result, the *NDCI* detected two of the collapsed pagodas. However, the pagoda enclosed by surrounding houses could not be detected. For the extracted area from the *Z* factor, some debris could be confirmed by comparing the pre- and post-event images although the building was still standing. For the location *b*, only the *NDCI* could detect collapsed buildings. Dharahara tower at the location *c*, was detected by all the indices. For the location *d*, about a half of buildings were collapsed. However, only the *NDCOI* and *Z* factor could detect as damage. Considering these results, the combination of the *NDCI* and *NDCOI* would be powerful for detecting affected areas with less false alarm.

5 **CONCLUSIONS**

The crustal movements and building damages caused by the 2015 Gorkha, Nepal earthquake were detected using two pre-event and one post-event ALOS-2 PALSAR-2 radar data. The geodetic deformation was estimated by the InSAR analysis using the phase information. Displacements of more than 1.5 m to the line-of -sight of the SAR observation were obtained by unwrapping the obtained coseismic fringes. However the deformation was distributed larger than the imaging area. Thus only the relative displacements could be estimated by the InSAR analysis.

The normalized difference coherence and correlation indices, and the Z-factor were used to detect the damaged areas in Kathmandu. Although vegetation and other non-urban areas were masked for each index before the detection, false alarms due to seasonal changes of vegetation could not be removed completely. Comparing with the Pleiades optical images, all the indices show the capability for the damage detection. However, there are many omissions if only applying one of those indices.

ACKNOWLEDGMENT:

The ALOS PALSAR-2 data used in this study are owned by Japan Aerospace Exploration Agency (JAXA), and are provided through the JAXA's PI workshop. The Pleiades images are owned by Airbus Defence and Space.

REFERENCES:

Brunner D., Lemoine G. and Bruzzone L. 2010. Earthquake damage assessment of buildings using VHR optical and SAR imagery. *IEEE Transactions on Geoscience and Remote Sensing*, 48(5), 2403–2420.

Costantini M. 1998. A novel phase unwrapping method based on network programming. *IEEE Transactions on Geoscience and Remote Sensing*, 36(3), 813-821.

Ito Y., Hosokawa M., Lee H. and Liu J.G. 2000. Extraction of damaged regions using SAR data and neural networks. *ISPRS2000, International Activities of Photogrammetry and Remote Sensing*, XXXIII(B1), 156–163.

Matsuoka M. and Yamazaki F. 2004. Use of satellite SAR intensity imagery for detection building areas damage due to earthquake. *Earthquake Spectra*, 20, 975–994.

Matsuoka M. and Yamazaki F. 2005. Building damage mapping of the 2003 Bam, Iran, Earthquake using Envisat/ASAR intensity imagery. *Earthquake Spectra*, 21, S285–S294.

Michel R., Avouac J.-P., and Taboury J. 1999. Measuring ground displacements from SAR amplitude image: Application to the Landers earthquake. *Geophysical Research Letters*, 26(27), 875-878.

Stramondo S., Cinti F.R., Dragoni M., Salvi S. and Santini S. 2002. The August 17, 1999 Izmit, Turkey, earthquake: Slip distribution from dislocation modeling of DInSAR and surface offset. *Annals of Geophysics*, 45(3/4), 527-536.

United States Geological Survey (USGS) 2015. http://earthquake.usgs.gov/earthquakes/eventpage/us20002926 #general_summary

Wang T.L. and Jin Y.Q. 2012. Postearthquake building damage assessment using multi-mutual information from pre-event optical image and postevent SAR image. *IEEE Geoscience and Remote Sensing Letters*, 9(3), 452–456.

Yonezawa, C., and Takeuchi, S. 2001. Decorrelation of SAR data by urban damages caused by the 1995 Hyogoken-Nanbu Earthquake. *International Journal of Remote Sensing*, 22(8), 1585–1600.